Insights into Ionic Transport and Structural Changes in Magnetite during Multiple Electron Transfer Reactions

Wei Zhang, David C. Bock, Christopher J. Pelliccione, Yan Li, Lijun Wu, Yimei Zhu, Amy. C. Marschilok, Esther S. Takeuchi, Kenneth J. Takeuchi, Feng Wang**

Dr. W. Zhang, Dr. D.C. Bock, Dr. C.J. Pelliccione, Dr. L. Wu, Prof. Y. Zhu, Prof. E.S. Takeuchi, Dr. F. Wang

Energy Sciences Directorate, Brookhaven National Laboratory, Upton, NY 11973, USA

E-mail: fwang@bnl.gov

Dr. Y. Li

American Physical Society, Ridge, NY 11961, USA

Dr. A. C. Marschilok, Prof. E.S. Takeuchi, Prof. K.J. Takeuchi

Department of Materials Science and Engineering, Stony Brook University, Stony Brook, NY 11974, USA

Dr. A. C. Marschilok, Prof. E.S. Takeuchi, Prof. K.J. Takeuchi

Department of Chemistry, Stony Brook University, Stony Brook, NY 11974, USA

E-mail: kenneth.takeuchi.1@stonybrook.edu

Metal oxides, such as Fe_3O_4, hold promise for future battery applications due to their abundance, low cost and opportunity for high lithium storage capacity. In order to better understand the mechanisms of multi-electron transfer reactions leading to high capacity in Fe_3O_4, a comprehensive investigation on local ionic transport and ordering is made by probing site occupancies of anions (O^{2-}) and cations (Li^+, Fe^{3+}/Fe^{2+}) using multiple synchrotron X-ray and electron-beam techniques, in combination with *ab-initio* calculations. Results from this study

provide the 1st experimental evidence that the cubic-close-packed (ccp) O-anion array in Fe_3O_4 is sustained throughout the lithiation and delithiation processes, thereby enabling multiple lithium intercalation and conversion reactions. Cation displacement/re-ordering occurs within the ccp O-anion framework, which leads to a series of phase transformations, starting from the inverse spinel phase and turning into intermediate rock-salt-like phases ($Li_xFe_3O_4$; $0<x<2$), then into a cation-segregated phase ($Li_2O \bullet FeO$), and finally converting into metallic Fe and Li_2O. Subsequent delithiation and lithiation processes involve interconversion between metallic Fe and FeO-like phases. The results from this study may offer new insights into the structure-determined ionic transport and electrochemical reactions in metal oxides, and those of other compounds sharing a *ccp* anion framework, reminiscent of magnetite.

Keywords: Batteries, High-capacity Electrodes, Multiple-Electron Transfer Reactions, Ionic Transport, Magnetite

1. Introduction

Lithium-ion batteries (LIBs) lead the consumer market of energy storage devices for portable electronics,[1] and the LIB market is expanding into power applications such as electric vehicles and the grid.[2] Future large-scale LIB designs could benefit from metal-cation based electrode materials capable of multiple electron transfers (MET) per metal-cation,[3] resulting in higher energy density compared to commonly employed intercalation-type electrodes.[4] Many electrode materials were reported to undergo MET reactions, such as metal oxides, fluorides, nitrides and sulfides, [4a-f] layered dichalcogenides, layered oxides, vanadyl phosphate, [4g, 4h] and also mixed-anion and cation compounds. [5a-c] Many of these electrode materials share a common feature in their structures, *i.e*. the close-packed anion framework with tetrahedral and octahedral sites being occupied by cations. The MET reactions in these materials very often involve both intercalation and conversion processes, leading to multiple phase transformations that can profoundly affect the rate capability and cycling stability.[6] Thus, a detailed mechanistic investigation is needed for better understanding of the complex MET reactions and associated structural changes.

Metal oxides of the general formula, M_3O_4, such as Fe_3O_4,[4b, 4d, 7] Co_3O_4,[8] and Mn_3O_4,[9] have been considered as possible MET redox compounds; although they share the same formulation and have similar metal oxidation states, Fe_3O_4 is an inverse spinel, Co_3O_4 is a spinel, and Mn_3O_4 is a tetragonally distorted spinel. For a spinel structure,

M^{2+} and M^{3+} cations are located in tetrahedral (8a) and octahedral (16d) sites of a cubic-close-packed (ccp) O-anion array, respectively, while for an inverse spinel, the tetrahedral site is occupied by one of the M^{3+} cations while the other M^{3+} cation and the M^{2+} cation occupy octahedral sites of a ccp O-anion array. These metal oxides are currently under active investigation for potential use as lithium insertion electrodes,[10] as well as conversion electrodes capable of delivering theoretically high capacities through full reduction of the transition metals.[1, 6a] One of the inverse spinel oxides, Fe_3O_4, has been intensely studied for battery applications, due to its low cost, natural abundance, and low toxicity.[6b] A recent review highlights the significance of the particle size and morphology of Fe_3O_4, as well as the role of the heterostructure encompassing the active material.[11] The mesoscale electrode environment of nanocrystalline Fe_3O_4, has also been recently evaluated, indicating the significant influence of agglomeration on functional capacity.[12]

The full electrochemical reduction of Fe_3O_4 results in the formation of metallic Fe and Li_2O.[13] However, the reduction process is actually complicated, involving multiple-phase transformations with a strong dependence on electrochemical conditions. As reported in previous X-ray diffraction (XRD) studies,[13a-c, 14] Fe_3O_4 firstly undergoes an intercalation process resulting in $Li_xFe_3O_4$ ($0 < x < 2$), and the corresponding phase was determined to accommodate up to two lithium ions per formula unit of Fe_3O_4 and possesses a partially ordered rock-salt structure.[13a, 13b, 14] However, the results from

other X-ray studies suggested different reaction pathways, leading to rock-salt FeO[15] or the rock-salt-like phase, Li_xFeO_2.[13d] A similar Li_xFeO_2 phase was also produced by discharging Fe_3O_4 at 400℃.[10b, 16] Therefore, there remains uncertainty about the transformation pathway during the multi-electron transfer reaction in Fe_3O_4, largely due to the challenge in identifying the structure of those lithiated materials that generally have poor crystallinity. In contrast to Fe_3O_4, the electrochemical reaction of α-Fe_2O_3 was thoroughly investigated,[4e-f] and much different electrochemical mechanisms in the two systems were suggested by these previous studies.

Coupled with complex structural evolution is electronic and ionic transport in Fe_3O_4 during MET reactions, another key property that governs the intrinsic rate capability of the electrode materials. Because Fe_3O_4 exhibits high electronic conductivity (2 x 10 $\Omega^{-1}m^{-1}$),[17] ionic transport, instead of electronic transport, may be kinetically limiting steps for the electrochemical reactions. But, during MET reactions lithium insertion into interstitial tetrahedral/octahedral sites in the ccp O-anion array inevitably induces Coulombic repulsive interactions between the Li ions and the Fe ions occupying neighboring tetrahedral or octahedral sites (when they share the same planes), which results in considerable energy barriers for ionic transport. More studies are needed to identify how Li and Fe ions migrate and relocate during MET reactions. Thus, a detailed kinetic and mechanistic study regarding the evolution of local chemical/structural ordering and dynamic processes of ionic transport, is necessary in order to gain insight

into the complicated electrochemistry associated with Fe_3O_4.

Bulk The general XRD characterization only provides averaged information on long-range ordering over large areas of agglomerates, without sufficient resolution of the local structural ordering and the heterogeneous electrochemical reactions within individual nanoparticles. Furthermore, the ordering of light elements, especially Li ions, in the intermediate phases is not well resolved by XRD. Scanning transmission electron microscopy (STEM), coupled with electron energy-loss spectroscopy (EELS) and electron diffraction has proven powerful in identifying structural and chemical ordering due to its extraordinary spatial resolution (down to the atomic level) and high sensitivity to the chemical states of both light elements (*i.e.*, Li) and transition metals.[18] The latest development of aberration-corrected annular-bright-field (ABF) imaging enables direct visualization of light elements, such as H in YH_2 [19] and Li in $LiFePO_4$.[20] In this study, ABF imaging, in combination with high angle annular-dark-field (HAADF) imaging and EELS, was applied to directly probe the statistical site occupancies of all of the involved anions (*i.e.* O^{2-}) and cations (Li^+, Fe^{2+}/Fe^{3+}) in the intermediate phases, providing detailed information about the ionic-diffusion pathways during lithiation/delithiation. The local coordination and bonding states of Fe were determined by X-ray absorption spectroscopy (XAS) and EELS at both the electrode and single-particle levels. Phase transitions and structural changes of Fe_3O_4 nanoparticles during MET reactions were determined by selected area electron diffraction (SAED). *First-principles* calculations

using density functional theory with the Hubbard correction (DFT+U) were employed to help elucidate the origin of the observed structural ordering, and the underlying mechanisms involved in the phase transitions and the kinetics of ionic transport. For the first time, we observed that the ccp O-anion array was maintained throughout the lithiation/delithiation process, thereby enabling multiple lithium intercalation and conversion reactions. Sluggish cation displacement and reordering (within the ccp O-anion framework) led to multiple phase transformations, involving several intermediates including highly structural-integrative rock-salt-like phase $Li_xFe_3O_4$ and cation-segregated $Li_2O•FeO$ *via* intercalation reactions, and a final metallic Fe phase *via* conversion reactions. Conversely, the MET delithiation reactions led to a FeO-like phase, instead of the original Fe_3O_4 phase. The dynamic processes of ionic transport and ordering are discussed based on the results obtained from local structural studies and DFT calculations.

2. Results

2.1 Multiple-electron transfer (MET) reactions in Fe_3O_4 Voltage profiles of the nano-Fe_3O_4/C electrode for the first three cycles (galvanostatic mode) is given in Figure 1a, indicating irreversible behavior during the 1st cycle, but with reversible behavior thereafter. The onset of the redox plateau in the first discharge (about 1.7 V) corresponds to intercalation of Fe_3O_4 with 0.5 electron equivalents.[13a] Further lithiation led to a

sloping region between 1.7- 1.0 V, before the 2nd electron equivalent, and then the subsequent long plateau at 0.9 V until about 6 electrons, which is followed with another sloping region with a gradual drop in voltage to 0.2 V. When the sample is charged to 3 V, the voltage profile was not symmetric to that of the discharge, with only about ½ of the capacity recovered; then the voltage profiles in the subsequent discharge and charge processes became similar, indicating a high cycling reversibility. The overall electrochemical behavior of the binder-free electrodes resembles that of electrodes containing binder when they were cycled at a low current (equivalent to C/80) (Figure S1).

The measurements using galvanostatic intermittent titration technique (GITT) type curves were performed for the Fe_3O_4 electrode, and a typical curve for the 1st cycle is given in Figure 1b. The voltage profile indicated large variation of the reaction kinetics (shown by the change of overpotential) at different states of lithiation and delithiation. The polarization was low at the beginning of the lithiation, and increased upon further lithiation (to 1.0 V), indicating a sluggish reaction process, likely due to the slow cation displacement/reordering and multiple phase transformations with lithium intercalation (as to be discussed below). The reaction kinetics is much improved during the following lithiation (*i.e.* long plateau below 0.9 V) and delithiation processes, as indicated by significantly reduced polarization. In order to understand the electrochemical behaviors

and associated reaction kinetics, detailed investigations were made to the structure of Fe_3O_4 and its evolution during MET reactions.

2.2 Structural evolution in individual Fe_3O_4 nanoparticles during MET reactions

Seven samples, one from a pristine electrode, five from discharged electrodes (to 0.6, 2, 4, 6, and 8 electron equivalents) and one electrode that was fully discharged and then fully-charged electrode, were used for this study (as indicated by red markers on the voltage profile in Figure 1a); the main results from high-resolution TEM imaging and electron diffraction measurements are provided in Figure 1 and Figure S2-4. As shown by the ADF images (Figure 1c), those as-synthesized Fe_3O_4 nanoparticles (sample A) are about 8-10 nm, and tend to form agglomerates. The structure of pristine materials was determined to be an inverse spinel phase (space group: Fd-3m (No. 227)) and the derived lattice constant of 8.4 Å is consistent with that reported by X-ray diffraction (JCPDS card No. 01-089-0691). No peaks corresponding to other phases were found in the diffraction patterns. One representative high-resolution HAADF image is given in the inset of A, indicating the single-crystallinity of the nanoparticle. As illustrated by the structure model for one unit cell of Fe_3O_4, the Fe_{8a}^{3+} atomic columns (weak contrast) are located at the 8a sites, and surrounded by four Fe/O columns (strong contrast) with the Fe and O atoms at the 16c and 32e sites, respectively.

Insertion of less than one Li^+ ion into Fe_3O_4 does not change the morphology of the particles (evidenced by the similarity between A and B). At this low level of lithiation, a

rock-salt-like phase $Li_xFe_3O_4$ ($0 < x < 1$) was formed with a similar structure as that of rock-salt FeO,[13a] in which the Fe atoms, initially sitting at tetrahedral sites, moved to octahedral sites.

After lithiation to 2 electron equivalents, the nanoparticles in sample C retain their uniform morphology (with no evidence of forming Fe; Figure 1c). However, the diffraction pattern of the 2 e^- sample changes dramatically, and only three peaks exist and they can be indexed to (111), (200), and (220) of the rock-salt-structured FeO phase (JCPDS card No. 0001-1223). This finding suggests that the FeO or FeO-like unit cells were already formed at 2 e^- reduction; but surprisingly no obvious change of the profile was found even at 4 electron equivalents (curve D in Figure 1d), and, correspondingly, the uniform morphology in sample D was sustained at such a high level of lithiation (Figure 1c). It should also be noted that no Li_2O was detected by electron diffraction at the 4 electron stage of lithiation.

At the lithiation state of 6 electron equivalents, very fine nanoparticles (~1 nm or smaller) were found in local areas, and further identified to be BCC Fe by SAED (E in Figures 1c, d), which is similar to the observation of conversion reactions in Fe_2O_3[21] and FeF_2.[22] Correspondingly, the diffraction peak of $Li_2O(111)$ and $Li_2O(220)$ started to emerge at 6e reduction (curve E in Figure 1d). Owing to the nanosize effect, the diffraction peaks of Fe phase were broad. The conversion reaction was inhomogeneous across the electrode, and some nanoparticles still remained in the intermediate FeO

phase. At the fully discharged state (8 electron equivalents), tiny nanograins, ~1 nm, were commonly observed across large areas of the sample (F in Figure 1c), and correspondingly, the diffraction pattern further confirmed that Fe and Li_2O became predominate phases (F in Figure 1d).

The typical morphology of the particles extracted from the fully charged sample is shown by the ADF image G in Figure 1c. The fine Fe nanograins became invisible and the particles appear to have coarsened. The intensity profile of the diffraction pattern suggests the formation of FeO-like phase, as indicated by the similarity of the curves D (for 4 e) and G (delithiated sample), but is completely different from that of the pristine Fe_3O_4 phase, labeled as A in Figure 1d. The reconversion into FeO-like nanoparticles was further confirmed by the EELS spectra of the oxygen K edge in Figure S3. In particular, the O K-edge spectrum of the delithiated Fe_3O_4 nanoparticles displays a much weaker prepeak at about 530 eV (compared to that of the pristine sample), suggesting the re-formation of a FeO-like phase.[23] The HAADF image recorded from a single de-lithiated nanoparticle in Figure S4 shows the crystalline structure of FeO-like phase. So all of the results led to the conclusion that, no Fe_3O_4, but FeO-like phase, was re-converted after the 1st cycle.

2.3 Evolution of the co-ordination and valence of Fe in Fe_3O_4 electrodes XAS measurements were made to Fe_3O_4 electrodes at several discharged states (Figure 2). The spectra for the X-ray absorption near-edge structure (XANES) of the Fe K-edge, shows a

gradual shift to lower energies (identified by the maximum of the first derivative of $\chi_\mu(E)$ for each spectrum), falling from 7126 eV in the pristine state to 7122 eV at 8.0 e^- reduction; the chemical shift indicates the electrochemical reduction of Fe from initial Fe^{3+}/Fe^{2+} to Fe^0/Fe^{2+} (Figure 2a). In addition, the pre-peak at about 7114 eV largely reflects the presence of tetrahedrally coordinated Fe in the initial Fe_3O_4, wherein the non-dipole (or quadrupole allowed) transition from 1s to 3d was induced by the distortion from centro-symmetry. [24] The magnitude of the pre-peak is slightly reduced in the 0.7 and 2.8 e^- discharged states, which is an indication of shifting Fe coordination geometry from tetrahedral to octahedral sites (of increased centro-symmetry). [24-25] Such a local shift may come from repulsion between Li and Fe ions sitting on the neighboring octahedral and tetrahedral sites of the same plane, as explained by Thackeray *et al*.[13a] At 4.0 e^-, this pre-peak is significantly suppressed (see Figure S5), and the edge position is shifted to about 7123 eV, indicative of a significant change in Fe oxidation state.

The Fourier transform of $\chi(k)$, $|\chi(R)|$ from extended X-ray absorption fine structure (EXAFS) for Fe is displayed in Figure 2b. The 1st peak at about 1.4 Å comes from the backscattering of neighboring oxygen atoms, while the 2nd broad peak between 2.0 - 3.5 Å contains multiple contributions, primarily from the nearest Fe coordination shell (Fe_T-Fe_T, Fe_T-Fe_O, Fe_O-Fe_O). Due to the similar distances for multiple paths (six paths within 0.2 Å of each other), the peaks combined from each contribution create one broad 2nd shell peak.

Theoretical models were used to fit the EXAFS data. Example fits for samples at 0.7 e^- and 8.0 e^- discharged states are shown in Figure 2c, and the detailed results for other discharge states are in Tables S1, S2 and Figure S6. From the pristine electrode to the 0.7 e^- discharged state, there is no clear change in the EXAFS profile compared to that of the original Fe_3O_4 structure, confirmed by modeling. At 2.8 e^-, there is a minor component with a FeO-like rock-salt structure, accounting for about 10-20% of the EXAFS spectrum. At 4.0 e^-, there is clear transition into a FeO dominant structure, as indicated by the shift in the average Fe-O bonding environment from the two distinct Fe-O interatomic distances at 1.79 ± 0.01 and 1.97 ± 0.01 Å in the 0.7 e^- state, to a single Fe-O distance of 2.06 ± 0.02 Å in the 4.0 e^- state. In addition, the Fe-Fe coordination environment between 2.0 – 3.5 Å transitions from three distinct Fe-Fe distances at 2.92 ± 0.01 Å, 3.42 ± 0.01 Å, and 3.52 ± 0.01 Å in the Fe_3O_4 structure to a single Fe-Fe interatomic distance of 3.06 ± 0.03 Å in FeO. This is indicated by a sharper 2nd shell peak in Figure 2b compared to the broad peak in the preceding discharged states.

The EXAFS spectra of the materials lithiated to 6 and 8 e^- were fit using a combination of FeO and metallic Fe crystal structures. There is clear observation of metallic Fe at 6 e^-, accounting for about 20% of the EXAFS profile. The formation of Fe at this electron level is consistent with observation by ADF and SAED (E in Figure 1c, d). At 8e^-, the metallic Fe content increases to about 50% of the observed spectrum. The two Fe-Fe interatomic distances (2.55 ± 0.02 Å and 2.94 ± 0.02 Å) derived from the

metallic Fe structure and their contribution to $|\chi(R)|$ are shown in Figure 2c and primarily correspond to the 2nd shell peak at about 2.5 Å. In both the 6 and 8 e^- spectra, the Fe-O and Fe-Fe interatomic distances determined at 4.0 e^- remained intact with minor fluctuations, suggesting the retention of a robust ccp O-ion framework in the intermediates throughout the multiple phases of the Li^+ reaction until the final stage of conversion into metallic Fe.

2.4 Local ionic displacement and ordering in the intermediates In the electrodes discharged to 2-4 electron equivalents, the intermediates containing rock-salt units were formed. However, the rock-salt structure generally does not allow for direct Li^+ intercalation. In order to better understand the Li^+ occupation and transport in the intermediates, atomic HAADF and ABF images were recorded from single nanoparticles in the samples discharged to 2 e^- and 4 e^- equivalents (**Figures 3** and **4**). The nanoparticles in the 2 e^- sample maintained a uniform structure (Figure S7). So atomic HAADF and ABF images were recorded from a single particle along [110] direction, and then the whole HAADF and ABF images (Figures S7b and c) were averaged based on a single unit cell of Fe_3O_4, to obtain statistically meaningful atomic arrangement of alternating Li, O and Fe columns along the [001] direction (Figure 3a,b). While the bright and dark spots in the averaged HAADF and ABF images correspond to the positions of Fe ions, respectively; the other spots with weaker contrast in the averaged ABF image reflect the positions of O and Li ions, which are well distinguished in the

averaged intensity profiles from the scan lines (marked by dash line in Figures 3a and b) in Figures 3c and d. The weak spots near the O columns indicate the occupancy of lithium ions in the tetrahedral sites, such as 8a, 48f, and 8b. Note that only very few 8b sites were occupied by Li^+, and most of 8b sites were empty, labeled by $\square_{8b}$ in Figure 3d. The occupation of the Li ions at the tetrahedral sites was also identified from the ABF image along the [100] direction (Figure S8).

Based on the intensity distribution, the structure of lithiated Fe_3O_4 at 2 e^- state was determined and illustrated in Figure 3e, indicating the ordering of Li ions within the ccp O-anion framework. As illustrated by the structural model (Figure 3e), some Fe columns fully consist of Fe_{16c} or Fe_{16d}, while other Fe columns are equally filled with Fe_{16c} and Fe_{16d}. However, the intensity of Fe columns appears to be uniform across the whole unit cell (Figure 3a and c), suggesting that the proportion of 16c sites occupied by Fe ions is the same as that of 16d sites. Such equal occupation of Fe ions at 16c and 16d sites makes the structure close to that of rock-salt, giving rise to the FeO-like phase as was detected by electron diffraction at 2 e^- (Figure 1d). Therefore, in comparison to the structure of $LiFe_3O_4$, in which all the 16d sites filled with Fe ions while the 16c sites are equally occupied by Li and Fe ions, further lithiation may have led to Fe migration from16d to 16c sites.

In the 4e^- sample, the HADDF image shows a uniform rock-salt structure projected along the [100] direction (Figures S9a,b), in which no metallic Fe clusters were detected.

A magnified HAADF image from a local region within the nanoparticle is presented in Figure 4a, in which all the bright spots represent the Fe/O columns (see also the illustration in the inset), while the Fe atoms remain at the octahedral sites. In comparison to the HAADF image, the ABF image from the same area presents some new features (Figure 4b). Besides the Fe/O columns with dark contrast, faint but distinct dark contrast can be observed in the tetrahedral sites (as marked by green dots). To clearly show these dark spots, the intensity of the whole HAADF and ABF images (in Figures 4a and b respectively) was averaged to one unit cell of Fe_3O_4. The averaged images are given in Figures 4c and d, respectively, along with the averaged intensity profiles in Figure 4e. In the ABF image, the weak reduction of intensity between Fe/O columns clearly demonstrates the presence of Li in the tetrahedral sites. The non-uniform intensity distribution in Figure 4e also indicates the presence of Li across the 1 X 1 cell, despite its inhomogeneous distribution. Therefore, the results suggest that, the further lithiation from 2 to 4 electron equivalents, led to the increase of Li occupancy at the tetrahedral sites, *i.e.*, firstly the 8a and 48f sites, and then the 8b sites.

With further lithiation (above 4 electron equivalents), ultrafine Fe nanograins were generated. To reveal the phase transition process between Fe and FeO, an atomic HAADF image was taken from the samples lithiated to 6 electron equivalents (**Figure 5**), revealing mixed Fe and FeO phases in some local regions. Interestingly, the converted ultrafine Fe grain has a coherent orientation relationship with neighboring FeO grains

(indicated by the Fast Fourier Transform (FFT) pattern; Figure 5b), and they were determined to align along the Fe [100] or FeO [110] direction, with a crystalline orientation relationship: Fe [100] // FeO [110] and Fe (002) // FeO (002). The lattice orientation relationship of the Fe and FeO crystallites is similar to that reported in previous work on the growth of FeO from iron upon oxidization.[26] Similar measurements were performed on the samples at 8 electron equivalents, indicating that more FeO was converted to Fe, with interfacial coherency between the two phases maintained throughout the reaction process (Figure S10).

The interfacial structure at the Fe/FeO boundary was further identified by the atomic HAADF image (Figure 5c) from local region marked by the white box in Figure 5a. A schematic illustration is given in Figure 5d to show the arrangement of Fe atoms near the interfaces of Fe/FeO. The iron atom columns of Fe nanograins are marked by yellow spots in the center of the HAADF image, while the surrounding iron atoms of the FeO matrix are labeled with red spots, which were obtained directly from two typical areas marked by the green and pink boxes in the image. Since the atomic distances and bonding angles in the (002) plane of Fe are comparable to those in the (002) plane of FeO (as illustrated in the blue box) with only ~ 6% lattice mismatch, these two phases match very well with each other at this interface. In the pink box, the orientation FeO [1-11] // Fe [011] was also observed around the other interface. The atomic configurations of planes FeO (1-11) and Fe (011) are illustrated in Figure S11, which shows that the lattice misfits

are about 6% along the [100] direction of Fe, and about 22% along the [11-1] direction. Although such large misfit might yield high interfacial energy between Fe and FeO, it can be accommodated by interfacial dislocations that were commonly observed (Figure S12).

3. Discussion

The results from multiple characterizations (by XAS, SAED, ADF, HAADF, ABF and EELS) on bulk electrode and single nanoparticles of Fe_3O_4, suggest that several intermediate phases were formed but with negligible structural/morphology changes below 4 electrons, followed by a conversion reaction leading to a significant morphology change with metallic Fe gradually formed. Assisted by DFT+U calculations, we propose the mechanisms of ionic transport and correlated phase transformations, in a direct correlation to MET reaction process in Fe_3O_4.

3.1 Ionic transport/ordering coupled with phase transformations One striking feature of MET reactions in Fe_3O_4 is that, despite complex phase transitions, the O-anion framework was sustained throughout the entire lithiation and delithiation process, as illustrated by the red lines linking each O ions in **Figure 6**. This ccp framework establishes a stable network of interconnected tetrahedra and octahedra to accommodate Li and Fe ions,[27] allowing the displacement/ordering of cations (Li^+, Fe^{3+}, Fe^{2+}) to take place within it in the sequential (de)lithiation steps.

i) The intercalation process of one Li^+ ion to form $LiFe_3O_4$ (Figures 6a-c)

$$(Fe)_{8a}(Fe_2)_{16d}O_4 + Li^+ + e^- \rightarrow (LiFe)_{16c}(Fe_2)_{16d}O_4 \quad (1)$$

In the inverse spinel structure of $Fe^{+3}(Fe^{+2}Fe^{+3})O_4$, the Fe^{+3} ions occupy the tetrahedral site (8a), while the mixed Fe^{+2} and Fe^{+3} ions are located at the octahedral site (16d), as shown in Figure 6a. At 1 electron equivalent, the lithium ions will occupy the interstitial octahedral sites (16c), as shown in Figure 6b. Because of the short distance of only 1.8 Å between Li_{16c}^+ and Fe_{8a}^{3+} in the neighboring tetrahedral sites (8a), the repulsive electrostatic force between the two displaces the Fe_{8a}^{3+} ions to adjacent 16c sites (Figure 6c). Correspondingly, the valence state of Fe_{8a}^{3+} is reduced, to Fe_{16c}^{2+}. Indeed, DFT+U geometry optimization of a starting structure with direct insertion of Li^+ at the 16c site, *i.e.*, $Li_{16c}Fe_{8a}(Fe_2)_{16d}O_4$, leads to severe lattice distortion and a substantially elongated distance of 2.5 Å between neighboring Li_{16c}^+ and Fe_{8a}^{3+},with the latter displaced into the octahedral sites with a reduced magnetic moment of 3.7 μ_B, consistent with the expected charge status of Fe^{2+}. The final structure, labeled as $LiFe_3O_4$ (I) in Figure S13, consists of tilted LiO_6 octahedrons, whereas the neighboring FeO_6 octahedrons are aligned perpendicularly. However, such a structure represents a local minimum-energy configuration as a result of the low symmetry of the starting structure. Instead, for a starting structure with both Li^+ and Fe^{3+} occupying the 16c sites (*i.e.* $(LiFe)_{16c}(Fe_2)_{16d}O_4$), the ccp O-anion framework is preserved in the final structure, labeled as $LiFe_3O_4$ (II) in Figure S13, with the total energy lowered by 0.8 eV per unit

formula of Fe_3O_4 compared to the former case. The magnetic moment of the Fe ions at the 16c site was also computed to be 3.7 μ_B. The volume was computed to expand by 2.5%, consistent with the 1% increase in Fe-O distances from 0 to 0.7 e^- measured from EXAFS (Table S1).

ii) The intercalation process of the 2nd Li^+ ion to form $Li_2Fe_3O_4$ (Figures 6c-d)

$$(LiFe)_{16c}(Fe_2)_{16d}O_4 + Li^+ + e^- \rightarrow (Li_2)_{8a/48f/8b}(Fe_3)_{16c/16d}O_4 \quad (2)$$

As reported previously, excess lithium ions can occupy tetrahedral sites (8a and 48f).[13a] This is also verified by our experimental results in Figure 3. Due to the strong repulsive electrostatic force between Li_{16c}^+ and Li_{8a}^+, directly inserting the 2nd Li^+ at the 8a site led to a severe distortion of lattice symmetry and the *ccp* O-anion framework, as shown from DFT+U calculations (labeled as $Li_2Fe_3O_4$ (I) in Figure S13). Therefore, Li_{16c}^+ would be forced to occupy the neighboring 48f or 8b sites, leaving behind empty 16c sites. It allows the redistribution of Fe ions between 16c and 16d sites through the empty 16c sites, leading to the equal occupation of Fe ions at 16c and 16d sites, as indicated by the uniform intensity of Fe ions in the averaged HAADF image (Figure 3a). In order to examine such a structural model, Fe ions were set to occupy ¾ of the 16c sites and ¾ of the 16d sites, whereas the Li ions are placed at the 8a sites and neighboring 8b sites halfway between Li^+_{8a} ions (labeled as $Li_2Fe_3O_4$ (II) in Figure S13). Indeed the final structure computed by DFT+U largely preserves the O-anion framework and the Li ions at the neighboring 8a (or 8b) site pair up, forming linear Li_{8a}-Li_{8a}…Li_{8b}-Li_{8b} chains of

interatomic distance of 1.9 Å and 6.2 Å, respectively. The lithium insertion is accompanied by a volume expansion of 15%, in excellent agreement with the 5% increase in Fe-O distances from 0.0 e^- to 2.8 e^- measured from EXAFS (Table S1). Another model ($Li_2Fe_3O_4$ (III) in Figure S13) with non-uniform distribution of Fe ions at 16d and 16c sites was calculated for comparison, and the final structure was found to be 2 eV per unit formula higher than that of $Li_2Fe_3O_4$ (II).

iii) Continuous intercalation of more lithium ions to form a composite $Li_2O \bullet FeO$ (Figures 6d-e).

$$(Li_2)_{8a/48f/8b}(Fe_3)_{16c/16d}O_4 + 2Li^+ + 2e^- \rightarrow 2Li_2O \bullet FeO + Fe \qquad (3)$$

According to the STEM-ADF observations (Figure 1c), the integrity of a uniform crystalline structure was retained for up to 4 electron equivalents. It suggests that the 3D ccp O-anion framework, with O bonded with either Fe or Li ions, remains unchanged during this step. In this framework, the excess lithium ions can occupy the tetrahedral sites (48f and 8b) during the following intercalation in $Li_2Fe_3O_4$, as evidenced by the ABF image in Figures 3b and 4d. However, owing to the repulsive electrostatic force between $Li_{48f/8b}^+$ and neighboring $Fe_{16c/16d}^{2+}$, the structure becomes more and more unstable with the increasing insertion of lithium ions, and these Fe_{16c}^{2+} ions are pushed away from their original 16c/16d sites. Because all the Fe ions have been determined to stay at octahedral sites by XAS measurements, it suggests that a local atomic rearrangement may have occurred within the unit cells to stabilize the structure, as

shown in Figures 6d. During this atomic rearrangement, the +2 oxidization state of Fe is maintained, suggesting that one Fe ion is replaced by two Li ions. Such atomic rearrangement would result in the segregation of Fe and Li ions in different local areas, with the growth of two domains, one of which has a rock-salt structure, while the other has Li_2O structure in which Li ions prefer to remain at tetrahedral sites (8a, 48f and 8b), as illustrated in Figure 6e. The possible formation of this proposed FeO-like structure would be consistent with the XAS (Figure 2) and SAED (Figure 1d) measurements of lithiated samples above 2 electron equivalents. The segregation of Li ions to form Li_2O domains is also supported by local structural analysis (Figure 4), which shows the inhomogeneous distribution of Li ions across the whole nanoparticle. Owing to the projected view in Figure 4, it is difficult to determine the thickness of Li_2O domains. However, because one unit cell of Li_2O is surrounded by 8b sites, taking up the 8b sites by lithium ions would allow the Li_2O domains to grow to a size larger than a unit cell. We note that the insertion of two more lithium ions should reduce the oxidization state of one Fe ion, to form metallic Fe. The XAS results showed that all the Fe atoms are located at octahedral sites, and no metallic Fe were detected in the 4 e^- sample (Figure S6 and Table S2), which seems to suggest the prohibition of the segregation of Fe^0 atoms. By considering the large lattice misfit at the interface between Li_2O and FeO domains (~6%), we propose that strain-induced large space at the interface may allow the Fe^0 atom to stay at the octahedral sites.

iv) Extra Li storage by conversion reactions, leading to metallic Fe (Figures 6e-f).

$$FeO + 2Li^+ + 2e^- \rightarrow Fe + Li_2O \quad (4)$$

With deep lithiation, lithium ions will further reduce FeO to metallic Fe^0, accompanied with the growth of Li_2O domain. According to the crystalline orientation relationship between Fe and FeO (Figures 5 and S10), this step takes place on the {100} plane of the FeO structure because of the small misfit (~6%) between these two planes.

v) Delithiation process through reconversion reaction (Figures 6f-g):

$$Fe + Li_2O \rightarrow FeO + 2Li^+ \quad (5)$$

According to the structure determined by SAED measurement (Figure 1d), the Fe ions occupied the octahedral sites of the O-anion array, forming the rock-salt FeO structure. Presumably, at the end of delithiation some Fe ions at the octahedral sites of FeO phase may be substituted by Li cations, forming $Li_xFe_{1-x}O$. A similar phenomenon was recently reported in the FeF_2 upon delithiation, wherein a rock-salt phase $Fe_xLi_{2-x}F_2$ was detected by pair distribution function (PDF) technique.[28] Therefore, the delithiated phase should be considered to possess a FeO-like structure but likely with lithium in the structure. Notably, in Fe_2O_3, the reconversion also led to formation of FeO, not Fe_2O_3,[21] which is similar to our observation concerning delithiation in the Fe_3O_4 system. As for morphological evolution, we note that the multiple ultrafine Fe nanograins are coalesced to form larger particles, Figure 1c(G). During coalescence, these ultrafine Fe nanograins may align along certain planes to achieve a low-energy configuration.[29] Given the

sufficiently small particle size (~ 1 nm), the increased diffusion coefficient will facilitate the movement of surface atoms to complete this process.[30] One possible driving force for coalescence is to reduce surface energy.[31]

3.2 Structure-determined ionic transport and electrochemical behaviors The structural stability of the electrode materials is critical to the practical application in batteries, to ensure good cycling performance and a long lifetime. During the first discharge of inverse spinel structure Fe_3O_4, the robust ccp O-anion framework was sustained throughout the lithiation process, which is supported by the retention of Fe-O and Fe-Fe coordination shown in Figure 2b. For example, rock-salt FeO can be described using Fd-3m (spinel) with O at 32e, and 16c and 16d being fully occupied by Fe, while all of the tetrahedral sites are empty. Li_2O can also be described by Fd-3m with O at 32e, and 8a, 8b and 48f being fully occupied by Li (in this case, all octahedral sites are empty). Such a ccp O-anion framework appears to be robust, as a result of low mobility of O anions relative to Li/Fe cations. Before the full conversion of FeO into metallic Fe, Li_2O domains were already generated within the O-anion framework but had coherent connection with FeO domains, assuring the integrity of the crystalline structure. Since Li_2O is an electrochemically inactive material, generating Li_2O domains inside the nanoparticles (not surrounding them), is important to maintaining the electrochemical reactivity of the nanoparticles. During the delithiation process, the ccp O-anion array provides a framework for reconversion back to the rock-salt FeO phase. The following

reversibility is reminiscent of other transition-metal oxides with a rock-salt structure, such as CoO, FeO, and NiO.[4e]

The reversibility of conversion reaction in transition metal oxides is similar to that found in metal fluorides although F^- anions were involved in the latter case.[4a, 18] It should be noted that, similar to the maintaining the ccp O-anion framework in metal oxides, a ccp F-anion framework is expected to retain during conversion and reconversion reactions in metal fluorides despite multiple phase transformation and local cation displacement and ordering. As suggested by recent PDF measurements by Ko et al.,[28] Fe may be incorporated into LiF forming a rock-salt phase (Li-Fe-F) during re-conversion, so we expect that Li-Fe-O, with Fe-O like rock salt structure may form in the delithiated Fe_3O_4 electrodes. To this end, we believe the conservation of the ccp anion framework is essential to reversibility of conversation/reconversion reaction in metal fluorides, oxides and even other spinel-type (or like) electrodes.

The inverse spinel oxides are characterized with a unique 3D framework for the fast diffusion of lithium. However, when the inverse spinel structure is turned into rock-salt-like phases, the ionic transport and reaction kinetics are altered. During step (i) of lithiation, the lithium ion diffusion takes place *via* the 8a + 16c network. However, when Li ions firstly migrate to 8a sites, it results in the formation of a metastable phase, $Li_{16c}Fe_{8a}(Fe_2)_{16d}O_4$. Transforming this $Li_{16c}Fe_{8a}(Fe_2)_{16d}O_4$ structure to the final $(LiFe)_{16c}(Fe_2)_{16d}O_4$ phase is necessary to overcome an energy barrier with a structural

rearrangement. During step (ii), the distorted structure may facilitate lithium's ionic transport, according *to ab initio* computations.[32] But in the subsequent lithiation, forming the Li_2O and FeO domains requires not only the diffusion of Li ions, but also Fe ions, being re-arranged between neighboring cells, which would also cause the increase of energy barriers. This sluggish displacement of ions in the plateau region of the first discharge becomes the limit for high-rate capability in spinel-type materials. After the formation of the cation-segregated Li_2O•FeO phase, the interface between Li_2O and FeO domains facilitates the diffusion of Li ions. Thus, the diffusivity would rise after this structural re-ordering, causing the decrease of polarization as observed in the GITT type test (Figure 1b). In general, the kinetics of the intercalation reaction is low, but an unexpected improvement in kinetics during conversion was found in this inverse spinel Fe_3O_4, which may be attributed to the unique structural ordering, particularly the formation of a Fe-FeO coherent network, facilitating the electronic and ionic transport.

4.Conclusion

In this work, we investigated the atomistic structural evolution in Fe_3O_4 during multiple electron transfer (MET) electrochemical reactions, using complementary synchrotron X-ray/TEM-EELS spectroscopy and imaging techniques and with assistance of *first-principles* calculations. The results from this study revealed that the MET reaction was enabled by the retention of the *ccp* O-anion framework throughout the whole

discharge and charge processes. It is within a robust *ccp* O-anion framework that local cation displacement/re-ordering occurred in response to the lithium insertion and extraction, which led to a series of phase transformations from inverse spinel, to rock-salt-like phases ($Li_xFe_3O_4$; $0<x<2$), then to cation-segregated phase ($Li_2O \bullet FeO$), and finally to Fe/Li_2O nanocomposite phase formation and then reconversion into a FeO-like phase. The findings from this study offered new insights into the structural origin of the ion transport and reaction kinetics in Fe_3O_4 electrodes, which provide a direct explanation for the reversibility and rate capability of the material during cycling.

Understanding the structural evolution of the active material upon discharge and charge as described here is an important first step toward ultimately designing practical full cells based on Fe_3O_4. Developing a mechanistic understanding of the side reactions leading to formation of solid electrolyte interphase (SEI) which contribute to irreversible capacity in Fe_3O_4 cells, including contributions to fade over extended cycling, is a topic of future study.

The observation is also fundamentally interesting, particularly in identifying the sustained ccp O-anion framework in Fe_3O_4 (despite multiple phase transformations), since it may also be relevant to other electroactive materials that possess a ccp anion framework, including metal oxides and fluorides. In combination with the insight provided by many previous studies, our model may prove to be a paradigm for further interpretation of previous battery work involving lithium intercalation and conversion reactions as well as for the rational design of new electrodes for high-energy Li-ion

batteries.

5. Materials and Methods

5.1 Synthesis Nanocrystalline Fe_3O_4 powders were prepared by a co-precipitation approach as previously reported. [33] Briefly, aqueous solutions of iron (III) chloride hydrate, and iron (II) chloride tetrahydrate were added dropwise to a stirred solution of degassed water and triethylamine. Samples were isolated by centrifugation, washed with deionized water, and dried under vacuum at 60°C.

5.2 Electrochemical tests Samples for STEM measurements were binder-free electrodes fabricated by mixing Fe_3O_4 powders with Super P carbon (1:1 ratio). Coin cells were constructed, using lithium-metal anodes and an electrolyte (1M $LiPF_6$ in 1:1 volume ratio of dimethyl carbonate and ethylene carbonate). The theoretical discharge capacity of 8 electron equivalents was defined as the complete discharge of the cathode to 0.2 V versus Li. The total capacity at this voltage includes the capacity of the conductive carbon black additive, and capacity due to the formation of SEI. The other discharged samples were obtained by discharging the cathode to voltages of 1.6 V, 1.0 V, 0.87 V, and 0.7 V, and were defined, respectively, as 0.6 e, 2 e, 4e, and 6e discharge levels. Charged samples were obtained after first discharge and then charge to an ending voltage of 3 V. Additional electrodes with a composition of 45% Fe_3O_4, 45% Super P, and 10% PVDF were cycled between 3.0 – 0.2 V for comparison with the binder-free

electrodes. GITT type measurements were performed by applying an intermittent current for 5 h followed by a 5-h relaxation period. All the cells were (dis)charged at the same rate of C/80.

5.3 Structural characterization by STEM-EELS The ADF images, ABF images, HAADF images, EELS data and SAED patterns were recorded in both a JEOL 2100F microscope and a JEOL ARM 200F microscope equipped with two spherical-aberration correctors, a cold-field-emission electron source and a high-resolution dual-EELS spectrometer. The discharged- and charged-coin cells were de-crimped right after completing the electrochemical reaction. The Fe_3O_4 materials for STEM measurements were dispersed in dymethyl carbonate and loaded on to a copper grid in the glovebox and then sealed in an Ar-filled bag for transferring to the TEM column to minimize air exposure. The ABF/HAADF images were obtained by averaging over multiple images, each of them was acquired from local regions corresponding to a unit cell of Fe_3O_4. Therefore, the averaged ABF/HAADF images show the statistical distribution of atomic positions.

5.4 XAS measurements XAS measurements were collected on Fe_3O_4 electrodes that were discharged to 0, 0.7, 2.8, 4, 6, and 8 e^-. Each EXAFS spectrum was background subtracted, aligned, merged, normalized and de-glitched using Athena.[34] The built-in AUTOBK algorithm was used to minimize the background below R_{bkg} = 1.0 Å. Theoretical models generated through FEFF6 [35] were utilized in modeling the

experimental data to yield detailed information about the local atomic environment around Fe atoms as a function of the discharged state. The theoretical models were generated from Fe_3O_4, [36] FeO [37] and metallic Fe [38] crystal structures. The fits were conducted in a k-range of 2 – 10 $Å^{-1}$ in k, k^2, and k^3 -weightings simultaneously, and in an R-range that fully encompassed both the 1st and 2nd shell peaks (either 1.0 – 3.5 Å or 1.0 – 3.0 Å). Each spectrum was fit using an appropriate model determined by the R-factor of the fit, along with the statistical significance of the variables used. Combinations of Fe_3O_4, FeO, and metallic Fe were initially used to fit all but the pristine discharged state. Phases that resulted in either unrealistic or statistically insignificant results were removed from the model.

5.5 DFT calculations Spin-polarized DFT+U calculations were carried out with the projected augmented wave method[39] implemented in the Vienna *ab initio* simulation package,[40] using the PBE exchange-correlation functional and a kinetic energy cutoff of 520 eV. A Hubbard U correction of U_{eff} = 5.3 eV was applied to the Fe *d* orbitals. The pristine and lithiated Fe_3O_4 crystal structure was modeled using Fd-3m primitive cell containing two Fe_3O_4 formula units, and the first Brillouin zone was sampled using a 4 × 4 × 4 *k*-mesh. For pristine Fe3O4, DFT+U calculations yielded a lattice parameter of a=8.5 Å (a_{exp}=8.4 Å), with computed magnetic moments of 4.3 μ_B for Fe^{3+} (opposite signs on tetrahedral and octahedral sites) and 3.7 μ_B for Fe^{2+} respectively.

Supporting Information. Electrochemistry measurements of general Fe_3O_4 electrodes

with binder, XAS data processing and extract coordination, bond information, original electron diffraction data, EELS data, ADF images, structural model of FeO and Fe, identified local dislocations, high-resolution HAADF image of the delithiated samples, and results of the DFT calculations, are included in Supporting Information. This material is available from the Wiley Online Library or from the author.

ACKNOWLEDGMENT

This work was supported as part of the Center for Mesoscale Transport Properties, an Energy Frontier Research Center supported by the U.S. Department of Energy, Office of Science, Basic Energy Sciences, under award #DE-SC0012673. Work at Brookhaven, including the use of the National Synchrotron Light Source I, was supported by the U.S. Department of Energy, Office of Science, Basic Energy Sciences, Use Facilities Division as well as Materials Science and Engineering Division under Contract No. DE-SC0012704. The authors gratefully acknowledge Dr. Melissa C. Menard for the original collection of the XAS data.

References

[1] J.-M. Tarascon, M. Armand, *Nature* **2001**, *414*, 359.

[2] M. Armand, J.-M. Tarascon, *Nature* **2008**, *451*, 652.

[3] X.-P. Gao, H.-X. Yang, *Energy Environ. Sci.* **2010**, *3*, 174.

[4] a) G. G. Amatucci, N. Pereira, *J. Fluorine Chem.* **2007**, *128*, 243; b) H. Liu, G. Wang, J. Wang, D. Wexler, *Electrochem. Commun.* **2008**, *10*, 1879; c) R. Malini, U. Uma, T. Sheela, M. Ganesan, N. Renganathan, *Ionics* **2009**, *15*, 301; d) T. Muraliganth, A. V. Murugan, A. Manthiram, *Chem. Commun.* **2009**, 7360; e) P. Poizot, S. Laruelle, S. Grugeon, L. Dupont, J. Tarascon, *Nature* **2000**, *407*, 496; f) D. Larcher, D.Bonnin, R.Cortes, I. Rivals, L.Personnaz, J.M. Tarascon, *J. Electrochem. Soc.* **2003** *150*, A1643; g) M. S. Whittingham, *Chem. Rev.* **2004**, *104*, 4271; h) M. S. Whittingham, *Chem. Rev.* **2014**, *114*, 11414.

[5] a) N. Pereira, F. Badway, M. Wartelsky, S. Gunn, G.G. Amatucci, *J. Electrochem. Soc.* **2009**, *156*, A407; b) F. Wang, S.-W. Kim, D.-H. Seo, K. Kang, L. Wang, D. Su, J. J. Vajo, J. Wang, J. Graetz, *Nat. Commun.* **2015**, *6,* 66688; c) S.W.Kim, N.Pereira, N.A. Chernova, F.Omenya, P. Gao, M.S.Whittingham, G.G. Amatucci, D. Su, F. Wang, *ACS nano*, **2015**, *9*, 10076.

[6] a) J. Cabana, L. Monconduit, D. Larcher, M. R. Palacin, *Adv. Mater.* **2010**, *22*, E170; b) S. Hussain, K. Hess, J. Gearhart, K. Geiss, J. Schlager, *Toxicol. In. Vitro*. **2005**, *19*, 975.

[7] a) P.-L. Taberna, S. Mitra, P. Poizot, P. Simon, J.-M. Tarascon, *Nat. Mater.* **2006**, *5*, 567; b) W.-M. Zhang, X.-L. Wu, J.-S. Hu, Y.-G. Guo, L.-J. Wan, *Adv. Funct. Mater.* **2008**, *18*, 3941.

[8] a) Z.-S. Wu, W. Ren, L. Wen, L. Gao, J. Zhao, Z. Chen, G. Zhou, F. Li, H.-M. Cheng, *ACS nano* **2010**, *4*, 3187; b) W.-Y. Li, L.-N. Xu, J. Chen, *Adv. Funct. Mater.* **2005**, *15*, 851.

[9] H. Wang, L.-F. Cui, Y. Yang, H. Sanchez Casalongue, J. T. Robinson, Y. Liang, Y. Cui, H. Dai, *J. Am. Chem. Soc.* **2010**, *132*, 13978.

[10] a) J. B. Goodenough, K.-S. Park, *J. Am. Chem. Soc.* **2013**, *135*, 1167; b) M. M. Thackeray, *J. Am. Chem. Soc.* **1999**, *82*, 3347.

[11] A. Bruck, C. Cama, C. Gannett, A. C. Marschilok, E. S. Takeuchi, K. J. Takeuchi, *Inorg. Chem. Front.* **2015**.

[12] a) K. W. Knehr, N. W. Brady, C. A. Cama, D. C. Bock, Z. Lin, C. N. Lininger, A. C. Marschilok, K. J. Takeuchi, E. S. Takeuchi, A. C. West, *J. Electrochem. Soc.* **2015**, *162*, A2817; b) K. W. Knehr, N. W. Brady, C. N. Lininger, C. A. Cama, D. C. Bock, Z. Lin, A. C. Marschilok, K. J. Takeuchi, E. S. Takeuchi, A. C. West, *ECS Transactions* **2015**, *69*, 7; c) D. C. Bock, K. C. Kirshenbaum, J. Wang, W. Zhang, F. Wang, J. Wang, A. C. Marschilok, K. J. Takeuchi, E. S. Takeuchi, *Acs Appl. Mater. Interfaces* **2015**, *7*, 13457.

[13] a) M. Thackeray, W. David, J. Goodenough, *Mater. Res. Bull.* **1982**, *17*, 785; b) J. Fontcuberta, J. Rodriguez, M. Pernet, G. Longworth, J. Goodenough, *J. Appl. Phys.* **1986**, *59*, 1918; c) T. Yamada, K. Morita, K. Kume, H. Yoshikawa, K. Awaga, *J. Mater. Chem. C* **2014**, *2*, 5183; d) M. C. Menard, K. J. Takeuchi, A. C. Marschilok, E. S. Takeuchi, *Phys. Chem. Chem. Phys.* **2013**, *15*, 18539.

[14] a) M. Thackeray, L. De Picciotto, A. De Kock, P. Johnson, V. Nicholas, K. Adendorff, *J. Power Sources* **1987**, *21*, 1; b) M. Islam, C. Catlow, *J. Solid State Chem.* **1988**, *77*, 180.

[15] M. Thackeray, J. Coetzer, *Mater. Res. Bull.* **1981**, *16*, 591.

[16] N. Godshall, I. Raistrick, R. Huggins, *J. Electrochem. Soc.* **1984**, *131*, 543.

[17] J. Coey, A. Berkowitz, L. Balcells, F. Putris, F. Parker, *Appl. Phys. Lett.* **1998**, *72*, 734.

[18] F. Wang, R. Robert, N. A. Chernova, N. Pereira, F. Omenya, F. Badway, X. Hua, M. Ruotolo, R. Zhang, L. Wu, *J. Am. Chem. Soc.* **2011**, *133*, 18828.

[19] R. Ishikawa, E. Okunishi, H. Sawada, Y. Kondo, F. Hosokawa, E. Abe, *Nat. Mater.* **2011**, *10*, 278.

[20] L. Gu, C. Zhu, H. Li, Y. Yu, C. Li, S. Tsukimoto, J. Maier, Y. Ikuhara, *J. Am. Chem. Soc.* **2011**, *133*, 4661.

[21] Y. Orikasa, T. Maeda, Y. Koyama, H. Murayama, K. Fukuda, H. Tanida, H. Arai, E. Matsubara, Y. Uchimoto, Z. Ogumi, *J. Am. Chem. Soc.* **2013**, *135*, 5497.

[22] W. Zhang, C. D. Bock, J. C. Pelliccione, Y. Li, L. Wu, Y. Zhu, C. A. Marschilok, J. K. Takeuchi, S. E. Takeuchi, F. Wang, *Submitted* **2015**.

[23] C. Colliex, T. Manoubi, C. Ortiz, *Phys. Rev. B* **1991**, *44*, 11402.

[24] a) G. Shulman, Y. Yafet, P. Eisenberger, W. Blumberg, *Proc. Natl. Acad. Sci.* **1976**, *73*, 1384; b) A. Roe, D. Schneider, R. Mayer, J. Pyrz, J. Widom, L. Que Jr, *J. Am. Chem. Soc.* **1984**, *106*, 1676; c) M. Wilke, F. Farges, P.-E. Petit, G. E. Brown, F. Martin, *Am.*

Mineral. **2001**, *86*, 714.

[25] T. E. Westre, P. Kennepohl, J. G. DeWitt, B. Hedman, K. O. Hodgson, E. I. Solomon, *J. Am. Chem. Soc*. **1997**, *119*, 6297.

[26] a) R. F. Mehl, E. L. McCandless, F. N. Rhines, *Nature* **1934**, *134*, 1009; b) L. Collins, O. Heavens, *Proc. Phys. Soc. Sect. B*. **1957**, *70*, 265; c) S. Corkovic, A. R. Pyzalla, *Mater. Corros*. **2004**, *55*, 341.

[27] M. Thackeray, *Nat. Mater.* **2002**, *1*, 81.

[28] J. K. Ko, K. M. Wiaderek, N. Pereira, T. L. Kinnibrugh, J. R. Kim, P. J. Chupas, K. W. Chapman, G. G. Amatucci, *Acs Appl. Mater. Interfaces* **2014**, *6*, 10858.

[29] P. Jensen, *Rev. Mod. Phys*. **1999**, *71*, 1695.

[30] D.-Q. Yang, E. Sacher, *Surf. Sci*. **2002**, *516*, 43.

[31] a) K. E. Lehtinen, M. R. Zachariah, *J. Aerosol. Sci*. **2002**, *33*, 357; b) M. R. Zachariah, M. J. Carrier, *J. Aerosol. Sci*. **1999**, *30*, 1139.

[32] J. Lee, A. Urban, X. Li, D. Su, G. Hautier, G. Ceder, *Science* **2014**, *343*, 519.

[33] a) S. Zhu, A. C. Marschilok, E. S. Takeuchi, K. J. Takeuchi, *Electrochem. Solid-State Lett*. **2009**, *12*, A91; b) S. Zhu, A. C. Marschilok, E. S. Takeuchi, G. T. Yee, G. Wang, K. J. Takeuchi, *J. Electrochem. Soc*. **2010**, *157*, A1158.

[34] a) M. J. Newville, *J. Synchrotron Radiat*. **2001**, *8*, 322; b) B. Ravel, M. J. Newville, *J. Synchrotron Radiat*. **2005**, *12*, 537.

[35] a) J. J. Rehr, J. Mustre de Leon, S. I. Zabinsky, R. C. Albers, *J. Am. Chem. Soc*. **1991**, *113*, 5135; b) J. Mustre de Leon, J. J. Rehr, S. I. Zabinsky, R. C. Albers, *Phys. Rev.* **1991**, *B44*, 4146.

[36] M. Fleet, *Acta Crystallogr., Sect. C: Cryst. Struct. Commun*. **1984**, *40*, 1491.

[37] E. R. Jette, F. Foote, *J. Chem. Phys*. **1933**, *1*, 29.

[38] Z. Basinski, W. Hume-Rothery, A. Sutton, *Proc. R. Soc. London, Ser. A* **1955**, *229*, 1179.

[39] E. D. Bloch, W. L. Queen, R. Krishna, J. M. Zadrozny, C. M. Brown, J. R. Long, *Science* **2012**, *335*, 1606.

[40] G. Kresse, J. Hafner, *Phys. Rev. B* **1994**, *49*, 14251.

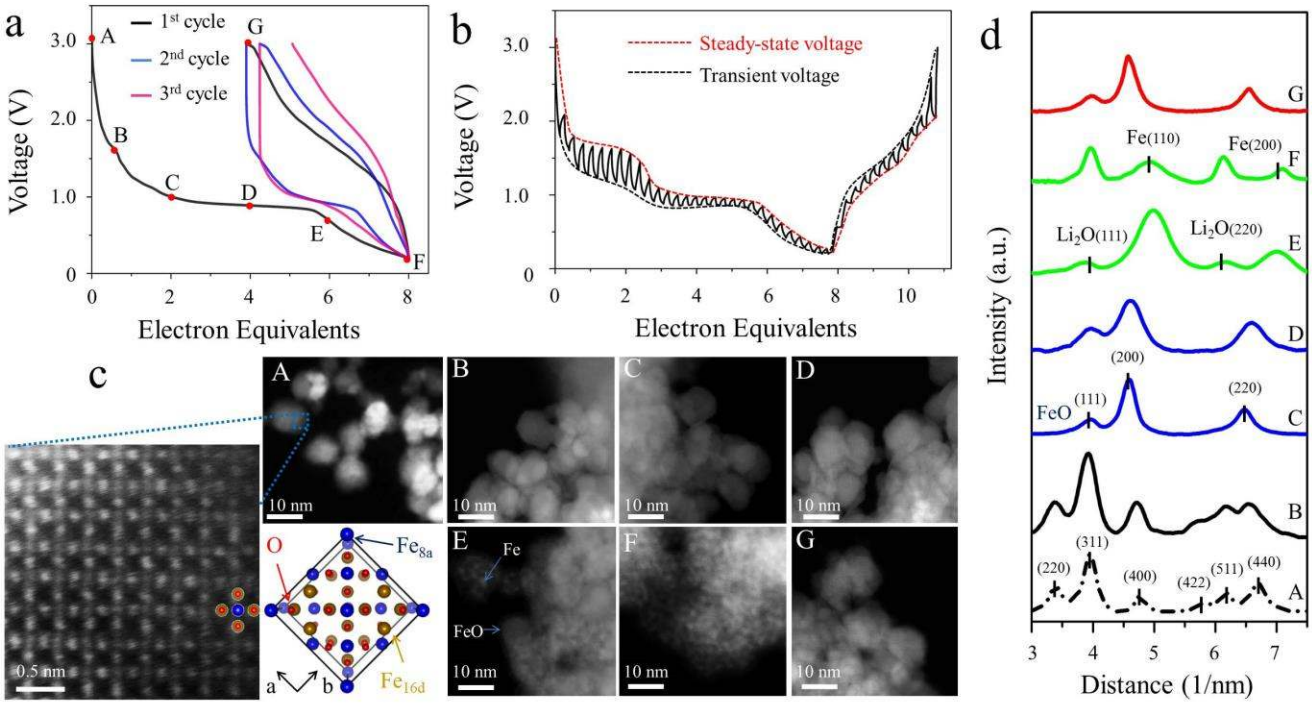

Figure 1. Multiple-electron transfer reactions and structural evolution in magnetite (Fe_3O_4) nanoparticles during discharge and charge. (a) Voltage profiles of the Fe_3O_4/C electrode during galvanostatic cycling (at a current rate equivalent to 1/80 C) and (b) voltage profiles from galvanostatic intermittent titration technique (GITT) measurements (at 1/80 C for 5 h followed by a 5 h rest), showing steady-state voltages (at quasi-equilibrium states; red dashed line), and transient voltages (black). (c) Representative annual dark-field (ADF) images of the (de)lithiated Fe_3O_4 nanoparticles recorded at different electron equivalents (as indicated in the voltage profiles). The inset in A shows a high-angle ADF image from the local area of a single Fe_3O_4 nanoparticle along [001] zone axis (marked by blue box in (A)), with a structural model of Fe_3O_4, where blue, brown and red spheres representing the Fe_{8a}, Fe_{16d} and O atoms, respectively. (d) Integrated intensity profiles of electron diffraction patterns (given in Figure S2), obtained from the regions of A-G in (c).

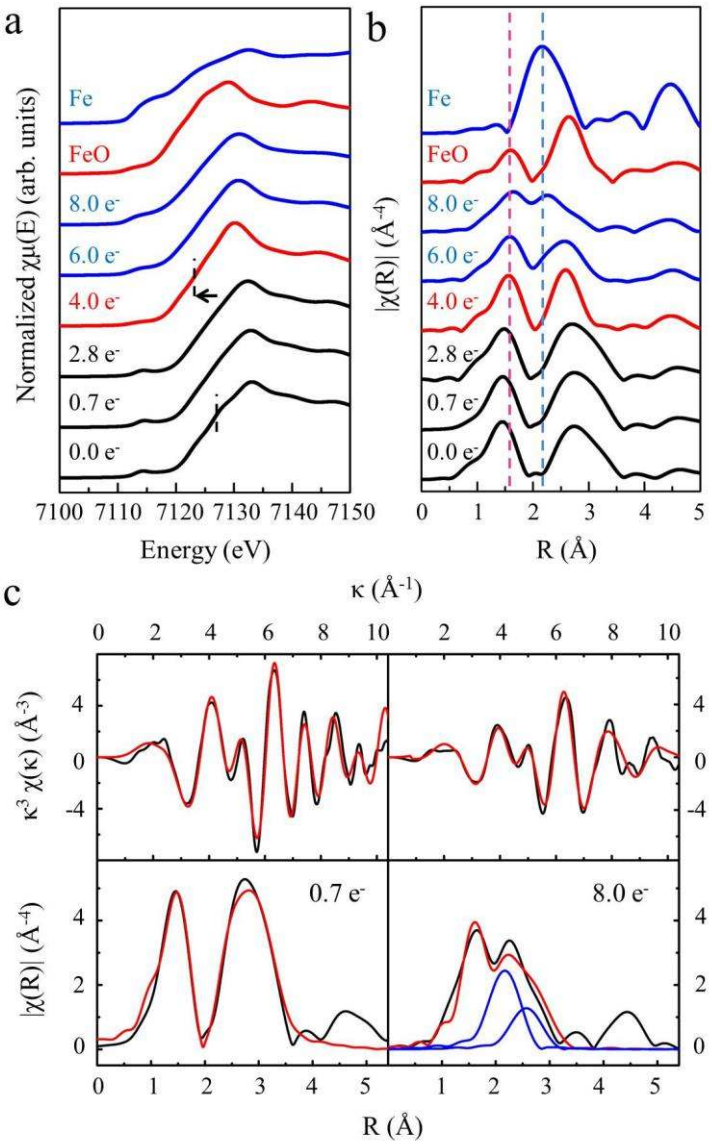

Figure 2. Local coordination and valence states of Fe in Fe_3O_4 discharged to certain electron equivalents. (a) X-ray absorption near-edge structure (XANES) of Fe K-edge, χ(E). The dashed black lines indicate the shift of energy positions after 4.0 e^- reduction. (b) The magnitude of k^3 weighted extended X-ray absorption fine structure (EXAFS), |χ(R)|. The vertical pink dashed line indicates characteristic features observed in the FeO structure while the vertical blue dashed line indicates features in metallic Fe. The red spectrum at 4.0 e^- indicates observation of FeO-like structure, and blue spectra (6.0 e^- and above) indicate observation of metallic Fe. (c) Examples of fitting for the samples at 0.7 e^- and 8.0 e^- discharged states. Black line represents experimental data and the red line is the corresponding fit in both |χ(R)| and k^3χ(k). Blue curves represent the metallic Fe-Fe contributions to the |χ(R)| spectrum.

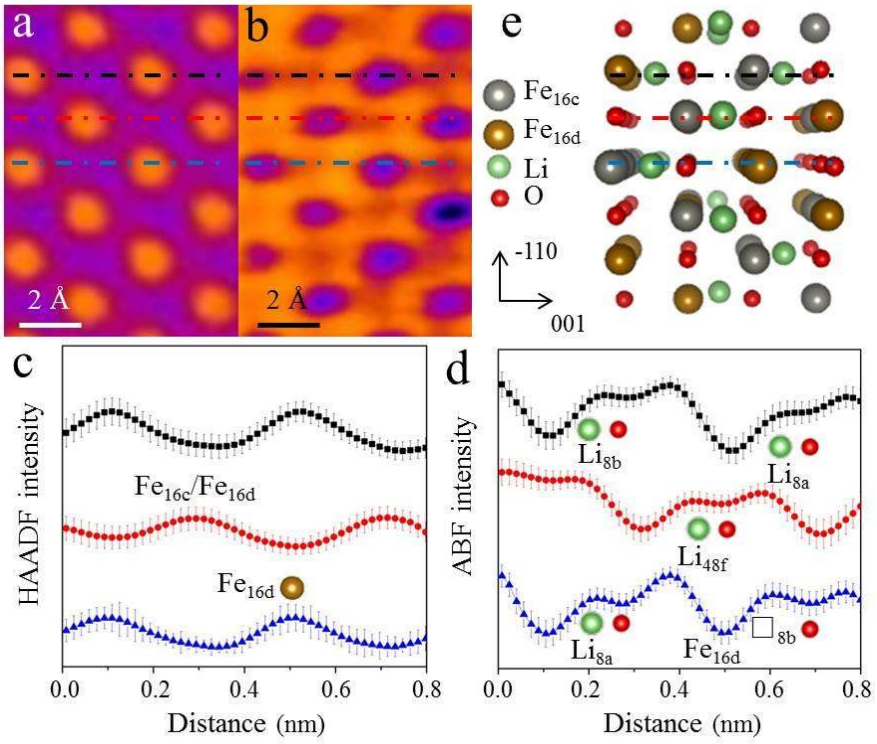

Figure 3. Ionic ordering within a single Fe_3O_4 nanoparticle discharged to 2 e^-. (a, b) Averaged HAADF and ABF images of lithiated Fe_3O_4 viewed along the [110] direction, showing different contrast between individual Fe, O, and Li columns, from which the atomic positions of anions (O^{2-}) and cations (Li^+, Fe^{2+}) were determined. (c, d) Intensity profiles from the line scan along the dash lines in (a, b), showing the Li occupation at the 8a, 48f, and 8b sites. The intensity peaks represent the positions of Fe ions in the HAADF image of (c), while the intensity valleys represent the positions of O^{2-} and Li^+ in the ABF image of (d). The presence of Li^+ ions is shown by the asymmetric distribution of intensity peaks around the O^{2-} ions (due to the lower scattering of Li^+ ions). The error bar was obtained from the original data in Figs. S7 b and c. The occupied and empty 8b sites were labeled as Li_{8b} and $□_{8b}$, respectively. The corresponding structural model (e), with gray, brown, green and red spheres representing Fe at 16c site, Fe at 16d site, Li, and O, respectively.

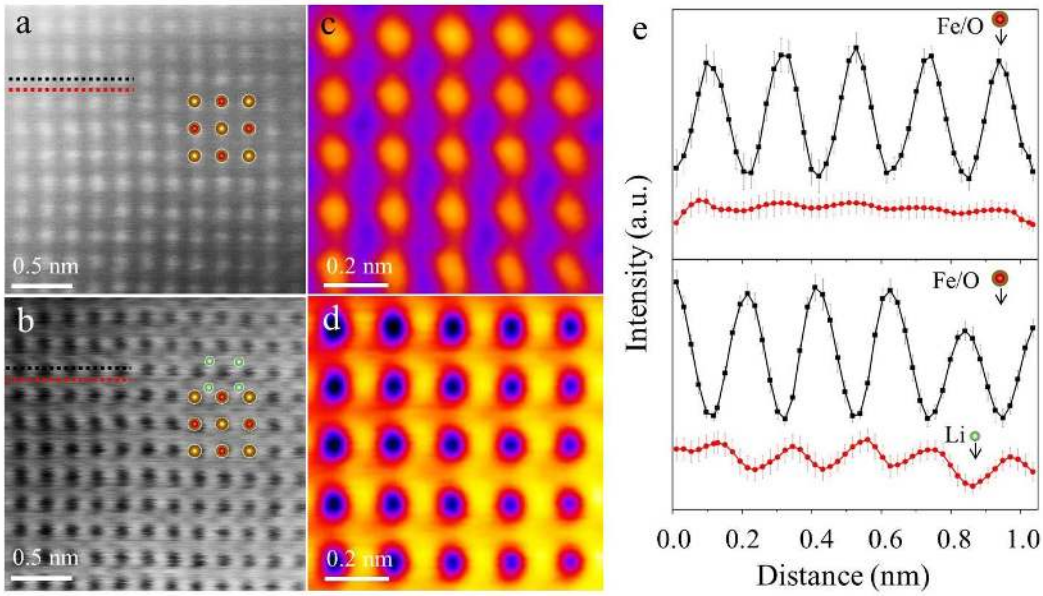

Figure 4. Ionic ordering within a single Fe_3O_4 nanoparticle discharged to 4 e^-. (a, b) HAADF- and ABF-images from a same local region of Fe_3O_4 particle, viewed along the [100] direction. Atomic occupancy is illustrated in the inset (with brown, red, and green spheres representing the Fe, O, and Li atoms respectively). (c, d) HAADF and ABF images averaged over one unit cell of Fe_3O_4. (e) Averaged intensity profiles from the line scan along the dashed lines in (a, b), showing the positions of the Fe/O and Li columns.

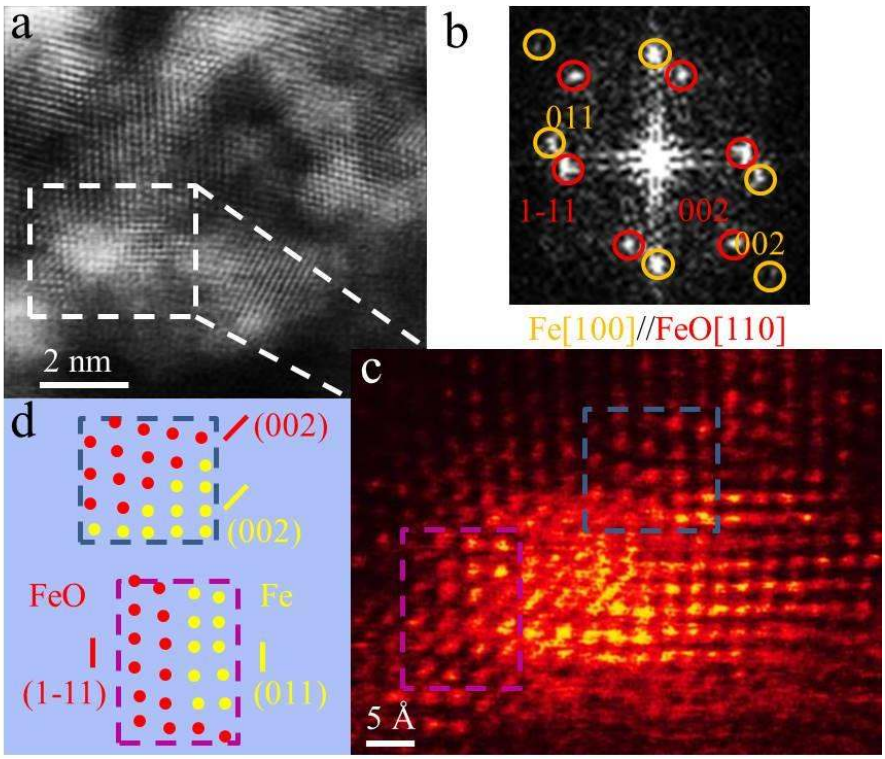

Figure 5. Structural correlation between converted Fe and FeO nanograins in the Fe_3O_4 electrodes discharged to 6 electron equivalents. (a, b) A HAADF image of the FeO/Fe nanoparticles, and corresponding FFT pattern produced from the region marked by the white box in (a), indicating the coherent orientation relationship between Fe and FeO. (c) A magnified HAADF image taken from the local region marked by white box in (a). A tiny BCC-structured Fe nanograin nucleated in the center of the image, is marked by yellow spots. (d) A schematic directly obtained from the interfacial areas marked by the blue and pink boxes in (c). The atomic arrangements at two different interfaces are clearly observed. The short red and yellow lines respectively represent the planes of Fe and FeO with the directions perpendicular to the page.

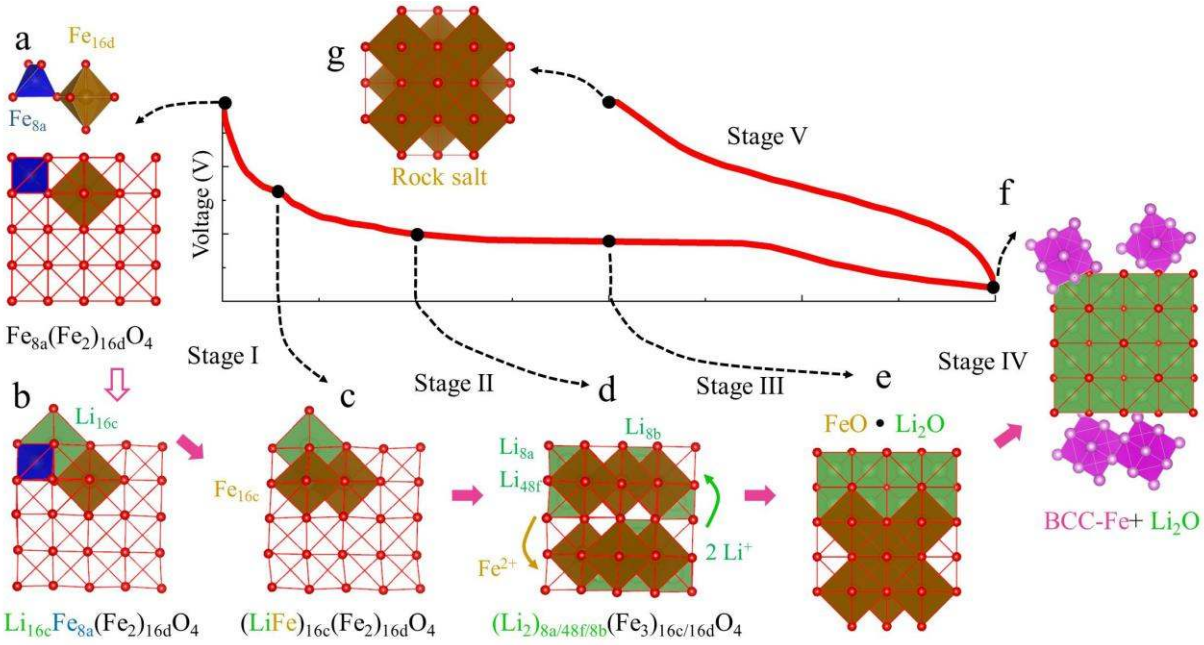

Figure 6 Schematic illustration of the ionic transport/ordering and resulting phase transformations in Fe_3O_4 during the 1st cycle. The O-anion array (red lines) provides the framework for the multiple lithium intercalation and reversible conversion processes with displacement/re-ordering of Li and Fe ions that lead to multiple phase transformations (from (a) to (g)). The Li occupation at 16c sites and the following atomic arrangement of Fe ions from 8a to 16c sites occur during stage I (a-c), After Li occupying 8a, 48f and 8b sites in stage II (c-d), segregation of Fe and Li ions led to Li_2O and FeO domains in stage III (d-e). FeO was finally converted to metallic BCC-Fe during stage IV (e-f), while reconversion back to FeO-like rock-salt structure took place during stage V (f-g). Blue, brown and pink colors are used to represent the different oxidization states of Fe ions, namely Fe^{3+}, Fe^{2+} and Fe^0.